Advances in High-Precision Amplifiers—The Extra L Opposed Current Converter

Erik Lemmen, *Student Member, IEEE*, Jan M. Schellekens, *Student Member, IEEE*, Cornelis G. E. Wijnands, and Jorge L. Duarte, *Member, IEEE*

***Abstract*—In existing half/full-bridge high-precision amplifiers, output distortion is present due to the required switch blanking time. The OCC topology does not require this blanking time but has a much higher total inductor volume compared to the half bridge. In this paper, a patented new topology is introduced that has the advantages of the OCC but with a much lower total inductor volume. The basic operation and properties of the ELOCC topology are explained including an extended optimization of the total inductor volume and an average model for control design. A prototype ELOCC current amplifier has been developed. The behavior of this prototype is in good agreement with the obtained simulation results. Even though the prototype is not fully optimized, the linearity compared to a full bridge is already impressive.**

***Index Terms*—DBI, dual-buck inverter, ELOCC, high precision, OCC, opposed current converter.**

I. Introduction

THE half bridge (HB) with output filter is a basic electronic building block used in high-frequency switching power converters and amplifiers. This topology, however, has some inherent problems that limit the performance, efficiency, and reliability. Consequently, the usability is reduced in high reliability and high-precision amplifiers. This problem becomes more prone at higher operating voltages, as higher voltage switches have worse switching characteristics.

Because two stacked switches are connected across the bus voltage, a blanking time (dead time) is required between switching OFF a transistor and switching ON the other transistor. The dead time must be sufficiently large to ensure that there is no overlap in conduction of both switches. During the dead time, the parallel diode of one of the two transistors is conducting and carries the filter inductor current. This results in a current-dependent switching node voltage during the dead time, which in turn introduces a zero-crossing distortion and significantly increases the total harmonic distortion of the output current.

In the case of MOSFETs, the parasitic body diode has poor switching characteristics resulting in high reverse recovery losses and increased electromagnetic interference (EMI).

Another problem of the HB is the sensitivity to cosmic radiation. This is mainly a problem in converters with a high bus voltage where MOSFETs are more sensitive to cosmic particle turn-on [1]. In case of a HB converter in operation, for the majority of the time, one of the MOSFETs is switched ON. If the opposite MOSFET is triggered by a cosmic particle, the bus voltage is shorted and both switches are typically destroyed. This sensitivity to cosmic radiation has a high impact on reliability.

There exists a topology that does not exhibit these downsides. This power converter topology is the opposed current converter (OCC) [2], [3] or dual-buck inverter (DBI) [4], shown in Fig. 1(a). The OCC or DBI topology is gaining popularity in grid-connected applications [5], [6] and for nondissipative voltage balancing in multilevel converter applications [7].

In the OCC, the bidirectional HB is replaced by two parallel-complementary unidirectional switching legs. Unfortunately, the resulting converter has a much higher magnetic volume and, therefore, higher cost of implementation, with respect to its conventional equivalent. Methods have been proposed to reduce the volume by coupling of inductors [8], [9] or using a split-wound inductor [10].

In this paper, a patented new topology is proposed that leads to a lower total inductor volume without applying coupled inductors. The new topology is named extra L opposed current converter, or ELOCC, and is an evolution of the existing OCC. The ELOCC, shown in Fig. 1(b), has no dead time distortion resulting in a high linearity compared to a half/full-bridge amplifier. Moreover, the diode can be optimized with respect to MOSFET parasitic diode resulting in reduced EMI.

II. Extra L Opposed Current Converter

The ELOCC topology is based on the existing OCC topology in which two parallel-complementary unidirectional switching legs together can provide bidirectional output current flow. In the OCC, in case the output current i_{out} is positive, the positive leg and filter inductor L_{f1} carries the output current. In case of negative output current, the negative leg and filter inductor L_{f2} carry the output current. Therefore, both filter inductors should be capable of conducting the full output current.

As proposed in [11], in order to avoid distortion on the output, a bias current should be added, flowing from the positive leg to the negative leg to keep both legs in continuous conduction mode (CCM).

In the ELOCC, an extra inductor L_b is added between the two unidirectional legs. The goal of this extra inductor is to balance the current through L_{f1} and L_{f2} such that each filter inductor conducts only half the output current. To balance the filter inductor currents, the average current through L_b should

Manuscript received July 17, 2014; revised October 23, 2014; accepted November 5, 2014. Date of publication November 10, 2014; date of current version May 22, 2015. Recommended for publication by Associate Editor R. Zane.

All the authors are with the Department of Electrical Engineering, Eindhoven University of Technology, 5612 AZ Eindhoven, The Netherlands (e-mail: e.lemmen@tue.nl; j.m.schellekens@tue.nl; c.g.e.wijnands@tue.nl; j.l.duarte@tue.nl).

Color versions of one or more of the figures in this paper are available online at http://ieeexplore.ieee.org.

Digital Object Identifier 10.1109/TPEL.2014.2369172

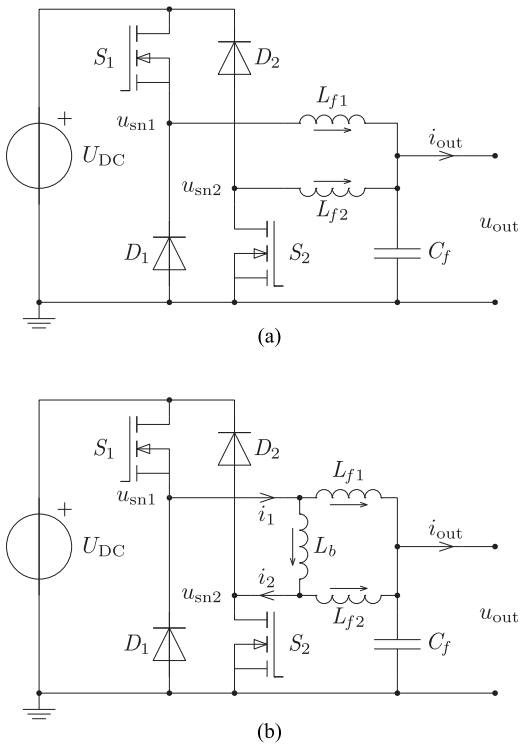

Fig. 1. Filtered half-bridge equivalent power converters. (a) OCC/DBI and (b) extra L OCC.

be controlled such that in the ideal case

$$\langle i_{L_b} \rangle = \begin{cases} \frac{1}{2} i_{\rm out} + i_{\rm offset}, & \text{for} \quad i_{\rm out} \geq 0 \\ -\frac{1}{2} i_{\rm out} + i_{\rm offset}, & \text{for} \quad i_{\rm out} < 0 \end{cases} \tag{1}$$

which can be simplified to

$$\langle i_{L_b} \rangle = \frac{1}{2} |i_{\rm out}| + i_{\rm offset}. \tag{2}$$

The brackets $\langle\,\rangle$ indicate the moving periodic average over a switching period. The term $i_{\rm offset}$ is an additional current component flowing from the positive to the negative leg. Note that the current through L_b is identical to the proposed modulated bias current in [11]. Since the current through L_b is identical to the OCC bias current, inductor L_b is also indicated as the bias inductor. Similar to the constant bias current in [11], the current through L_b can also be set to a constant value.

The current ripple of each of the filter inductors is assumed to be fully absorbed by the filter capacitor and $\langle i_{C_f} \rangle$ is assumed zero for subsequent analysis.

A. Converter Basics

The ELOCC switching cell contains two switches. These two switches give a total of four output states as given in Table I with the corresponding bias and average voltage. When a switch is OFF, the complementary diode is assumed to be conducting. The average voltage $u_{\rm avg}$ is defined as the average voltage of both switching nodes $u_{\rm sn1}$ and $u_{\rm sn2}$. The bias voltage $u_{\rm bias}$ is defined as the voltage between $u_{\rm sn1}$ and $u_{\rm sn2}$.

TABLE I
ELOCC STATE VOLTAGES

State	Switch S_2	Switch S_1	$u_{\rm avg}$	$u_{\rm bias}$
s_0	OFF	OFF	$\frac{1}{2}U_{\rm DC}$	$-U_{\rm DC}$
s_1	OFF	ON	$U_{\rm DC}$	0
s_2	ON	OFF	0	0
s_3	ON	ON	$\frac{1}{2}U_{\rm DC}$	$U_{\rm DC}$

A closer look at Table I reveals that in states s_0 and s_3, the bias voltage $u_{\rm bias}$ can be set to $U_{\rm DC}$ or $-U_{\rm DC}$, while the average voltage $u_{\rm avg}$ remains constant. In the states s_1 and s_2, the average voltage $u_{\rm avg}$ can be set to 0 V or $U_{\rm DC}$, while $u_{\rm bias}$ remains at 0 V. This means that $u_{\rm avg}$ and $u_{\rm bias}$ are decoupled. Therefore, a similar decomposition as done in [11] can be applied for the ELOCC as

$$u_{\rm avg} = \frac{1}{2}(u_{\rm sn1} + u_{\rm sn2}) \tag{3a}$$

$$u_{\rm bias} = u_{\rm sn1} - u_{\rm sn2} \tag{3b}$$

$$i_{\rm out} = i_{L_{f1}} + i_{L_{f2}} - i_{C_f} \tag{3c}$$

$$i_{\rm bias} = i_{L_b} + \frac{1}{2}(i_{L_{f1}} - i_{L_{f2}}) \tag{3d}$$

similar the switching node voltages can be expressed in terms of the bias and output voltage set points

$$u^*_{\rm sn1} = u^*_{\rm out} + \frac{1}{2} u^*_{\rm bias} \tag{4a}$$

$$u^*_{\rm sn2} = u^*_{\rm out} - \frac{1}{2} u^*_{\rm bias}. \tag{4b}$$

In steady state, the output voltage $u_{\rm out}$ is equal to the average voltage $u_{\rm avg}$, when neglecting losses.

Because L_b is actually in parallel to the series connection of L_{f1} and L_{f2}, a portion of $i_{\rm bias}$ will also flow through the filter inductors based on the impedance of the bias and filter inductors. Ideally, the inductors are chosen such that the portion of the bias current through the filter inductors ($\frac{1}{2}(i_{L_{f1}} - i_{L_{f2}})$) is very small and can be neglected.

The filter inductors in the ELOCC are designed to allow a certain peak current ripple. When assuming the output capacitor is large and the converter is in steady state, the peak current ripple amplitude is found to be

$$\hat{\Delta} i_{Lfk} = \frac{U_{\rm DC}}{8 L_{fk}} T_{sw} \tag{5}$$

where $k \subset \{1, 2\}$. The peak current ripple is typically chosen between 10% and 40% of $\hat{i}_{\rm out}$. With the filter inductors fixed, the filter capacitor C_f is determined. The output filter cutoff frequency f_o is defined by

$$f_o = \frac{1}{\pi \sqrt{2 L_f C_f}} \tag{6}$$

where $L_f = L_{f1} = L_{f2}$. The cutoff frequency of the output filter is typically chosen at $\frac{1}{5}$th of the switching frequency.

To have an output filter performance equivalent to the conventional HB, the filter capacitor can be kept identical to the HB filter capacitor, and the filter inductors should be chosen such that

$$L_f = 2L_{\mathrm{HB}} \tag{7}$$

where L_{HB} is the corresponding half-bridge filter inductor.

The choice for the bias inductor L_b is described in Section III. For now the inductance value of L_b is considered much smaller than L_f.

B. Bias inductor current

The relation between the periodic average switching node voltage $\langle u_{\mathrm{sn}k}\rangle$ and switch duty cycle δ_{S_k} of a unidirectional switching leg becomes linear, when the switch resistances are matched and the leg is operated in CCM, as shown in [12]. In the ELOCC switching cell, where two inductors are connected to a single leg, CCM is not obvious. Therefore, CCM is defined for the total current out of leg 1, i_1, and the total current into leg 2, i_2. In order to operate each of the legs in CCM, the currents i_1 and i_2 must be positive, resulting in the following bounds for the inductor currents

$$i_{L_{f1}} + i_{L_b} > 0 \tag{8a}$$

$$-i_{L_{f2}} + i_{L_b} > 0. \tag{8b}$$

Due to the current ripple Δi_{Lfk} in the filter inductors and Δi_{Lb} in the bias inductor, the following requirements apply for CCM

$$\frac{1}{2}i_{\mathrm{out}} - \Delta i_{Lf1} + \frac{1}{2}|i_{\mathrm{out}}| + i_{\mathrm{offset}} - \Delta i_{Lb} > 0 \tag{9a}$$

$$-\frac{1}{2}i_{\mathrm{out}} - \Delta i_{Lf2} + \frac{1}{2}|i_{\mathrm{out}}| + i_{\mathrm{offset}} - \Delta i_{Lb} > 0. \tag{9b}$$

To ensure that the converter is operated in CCM, i_{offset} is chosen such that

$$i_{\mathrm{offset}} \geq \hat{\Delta} i_{Lfk} + \hat{\Delta} i_{Lb}. \tag{10}$$

Typically, i_{offset} is chosen larger than $\hat{\Delta} i_{Lfk} + \hat{\Delta} i_{Lb}$ to guarantee CCM during transients.

C. Switching Waveforms

The steady-state switching waveforms for positive output current of the ELOCC power stage are shown in Fig. 2. The MOSFETs and diodes are considered ideal, the output capacitor is assumed large, and the bias inductor L_b is assumed to have a series resistance.

1) Time Interval t_0: The system is in output state s_2. The current in the filter inductors L_{f1} and L_{f2} decays with a rate of $\frac{u_{\mathrm{out}}}{L_{fk}}$. The current bias inductor decays exponentially due to the parasitic resistance of the inductor.

2) Time Interval t_1: During time interval t_1, the system is in output state s_3. The current in filter inductor L_{f1} increases with a rate of $\frac{U_{\mathrm{DC}}-u_{\mathrm{out}}}{L_{f1}}$, and the current in L_{f2} decays with a rate of $\frac{u_{\mathrm{out}}}{L_{f2}}$. The current in the bias inductor L_b increases with a rate of $\frac{U_{\mathrm{DC}}}{L_b}$. In case a negative voltage across the bias inductor L_b is required, the system is in output state s_0. Then the current in filter inductor L_{f1} decays with a rate of $\frac{u_{\mathrm{out}}}{L_{f2}}$ and the current in L_{f2} increases with a rate of $\frac{U_{\mathrm{DC}}-u_{\mathrm{out}}}{L_{f1}}$. The current in the bias inductor L_b then decreases with a rate of $\frac{U_{\mathrm{DC}}}{L_b}$.

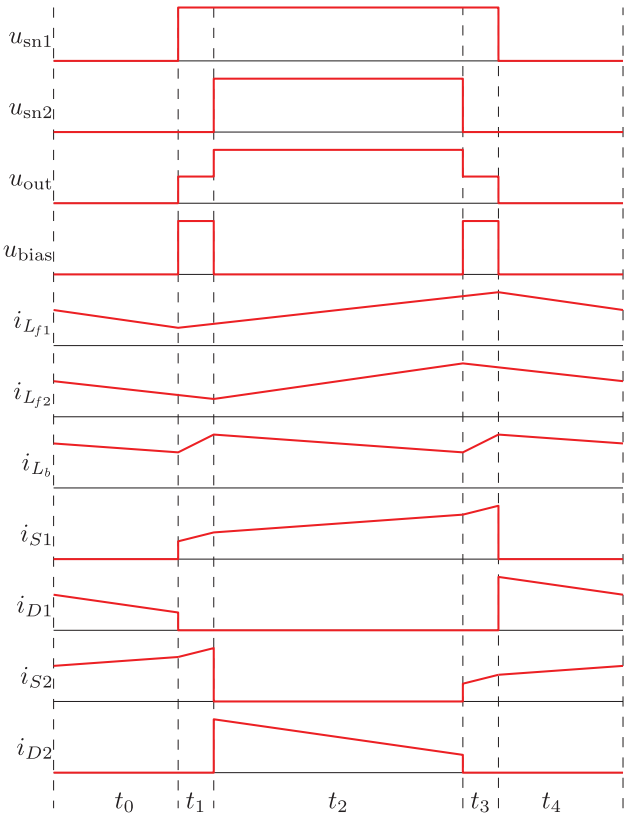

Fig. 2. ELOCC example steady-state switching waveforms.

3) Time Interval t_2: The system is in output state s_1. The current in the filter inductors L_{f1} and L_{f2} increases with a rate of $\frac{U_{\mathrm{DC}}-u_{\mathrm{out}}}{L_{fk}}$. The current through the bias inductor decays exponentially due to the parasitic resistance of the inductor.

4) Time Interval t_3: Identical to t_1.

5) Time Interval t_4: Identical to t_0.

III. Inductor Volume Optimization

In this section, the total inductor volume for an ELOCC power stage is compared to a conventional HB. The inductor volume is expressed as a function of L_b and R_{Lb}. The estimation of the inductor volume is done using the area-product method [13].

To simplify calculations, a few assumptions are made. The output current i_{out} is assumed to be sinusoidal and in phase with the output voltage. The current through the filter inductors $i_{L_{f1}}$ and $i_{L_{f2}}$ is assumed to be sinusoidal with a triangular current ripple, and the frequency of the output current is assumed much lower than the switching frequency. The bias current is set to a constant value, and it is assumed that there is no ripple in the output current for both the ELOCC and HB case.

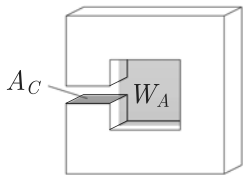

Fig. 3. Area-product parameters.

For a proper comparison between the ELOCC and HB, the ELOCC filter inductors are chosen according to (7).

A. Area-Product

The area-product A_P is the product of the winding area W_A and effective core area A_C, both indicated in Fig. 3. The volume of the inductor is then given by $V_L = K_{\mathrm{vol}} A_P^{0.75}$, where K_{vol} is the geometrical constant of the core shape. Since the total inductor volume of the ELOCC power stage, relative to the inductor volume of the HB is desired, the geometrical core constant K_{vol} is assumed equal for all inductors. As K_{vol} is assumed equal for the considered inductors, it can be omitted. This gives

$$V_L \propto A_P^{0.75} \tag{11}$$

which is sufficient for determining the relative inductor volume.

When it is assumed that all energy is stored in the core material of the filter inductor, so there is no leakage flux, the area-product of the HB filter inductor is given by

$$A_{P\mathrm{HB}} = \frac{L_{\mathrm{HB}}}{\hat{B} J K_{\mathrm{u}}} |\hat{i}_{L_{\mathrm{HB}}}| I_{L_{\mathrm{HB}}} \tag{12}$$

with $\hat{B}$ being the peak magnetic flux density, J is the RMS current density, and K_{u} is the window utilization factor. The currents $\hat{i}_{L_{\mathrm{HB}}}$ and $I_{L_{\mathrm{HB}}}$ are the respective filter inductor peak and RMS currents. The currents are given by

$$|\hat{i}_{L_{\mathrm{HB}}}| = |\hat{i}_{\mathrm{out}}| + \hat{\Delta} i_{L_{\mathrm{HB}}} \tag{13a}$$

$$I_{L_{\mathrm{HB}}} = \sqrt{\frac{1}{2}\hat{i}_{\mathrm{out}}^2 + \frac{1}{3}\hat{\Delta} i_{L_{\mathrm{HB}}}^2} \tag{13b}$$

where the peak inductor ripple current $\hat{\Delta} i_{L_{\mathrm{HB}}}$ can be expressed in terms of the peak output current $\hat{i}_{\mathrm{out}}$ as

$$\hat{\Delta} i_{L_{\mathrm{HB}}} = 2 k_{\mathrm{r}} \hat{i}_{\mathrm{out}} \tag{14}$$

where $2k_{\mathrm{r}}$ is used because the ripple coefficient k_{r} is defined for the ELOCC filter inductors [see (18a)].

Substituting (7), (13), and (14) into (12) gives

$$A_{P\mathrm{HB}} = \frac{L_f}{2\hat{B} J K_{\mathrm{u}}} \hat{i}_{\mathrm{out}}^2 (1 + 2k_{\mathrm{r}}) \sqrt{\frac{1}{2} + \frac{1}{3}(2k_{\mathrm{r}})^2}. \tag{15}$$

In the ELOCC switching cell, the total volume is determined by the volume of the three inductors together. Therefore, the area-product must be calculated for each of the inductors separately. The total relative inductor volume of the ELOCC switching cell is

$$\frac{V_{L\mathrm{ELOCC}}}{V_{L\mathrm{HB}}} = \frac{A_{PLf1}^{0.75} + A_{PLf2}^{0.75} + A_{PLb}^{0.75}}{A_{P\mathrm{HB}}^{0.75}} \tag{16}$$

where due to symmetry the area-product $A_{PLf1} = A_{PLf2}$. The peak magnetic flux density $\hat{B}$, current density J, and winding utilization factor K_{u} are set equal for all considered inductors.

Similar to (12), the area-product for the filter inductors is calculated. The peak and RMS filter inductor currents are given by

$$|\hat{i}_{L_{fk}}| = \frac{1}{2}|\hat{i}_{\mathrm{out}}| + \hat{\Delta} i_{Lfk} + Q_{\mathrm{Lf}} i_{\mathrm{bias}} \tag{17a}$$

$$I_{L_{fk}} = \sqrt{\frac{1}{8}\hat{i}_{\mathrm{out}}^2 + \frac{1}{3}\hat{\Delta} i_{Lfk}^2 + Q_{\mathrm{Lf}}^2 i_{\mathrm{bias}}^2} \tag{17b}$$

where again, the currents can be expressed in terms of the peak output current $\hat{i}_{\mathrm{out}}$ as

$$\hat{\Delta} i_{Lfk} = k_{\mathrm{r}} \hat{i}_{\mathrm{out}} \tag{18a}$$

$$i_{\mathrm{offset}} = k_{\mathrm{o}} \hat{i}_{\mathrm{out}}. \tag{18b}$$

The term $Q_{\mathrm{Lf}} i_{\mathrm{bias}}$ is the portion of the bias current that is flowing through the filter inductors, in which Q_{Lf} is a constant between 0 and 1 that is defined later. The constant bias current is described by

$$i_{\mathrm{bias}} = \frac{1}{2}|\hat{i}_{\mathrm{out}}| + i_{\mathrm{offset}} = \hat{i}_{\mathrm{out}} \left(\frac{1}{2} + k_{\mathrm{o}} \right). \tag{19}$$

The resulting area-product of the filter inductors, using (17), (18), and (19), is

$$A_{PLf}k = \frac{L_f}{\hat{B} J K_{\mathrm{u}}} \hat{i}_{\mathrm{out}}^2 \left(\frac{1}{2} + k_{\mathrm{r}} + Q_{\mathrm{Lf}} \left[\frac{1}{2} + k_{\mathrm{o}} \right] \right) \times \sqrt{\frac{1}{8} + \frac{1}{3}k_{\mathrm{r}}^2 + Q_{\mathrm{Lf}}^2 \left(\frac{1}{2} + k_{\mathrm{o}} \right)^2}. \tag{20}$$

Also, similar to (12), the area-product for the bias inductor is determined for constant bias current operation. In [14], it is assumed that the current through the bias inductor has no ripple, this results in an infinitesimal inductor as optimal solution (minimum total volume). In practice, however, a positive average bias voltage is required to compensate for the voltage drop in the bias path. As a result of this, an average voltage across the bias inductor is required. Because $\langle u_{\mathrm{bias}} \rangle \neq 0$, there is a ripple in the bias inductor current as shown in Fig. 4. This ripple becomes larger as the inductor becomes smaller resulting in a different optimal value for the bias inductor.

The current ripple in the bias inductor is composed of two components. The basic current ripple Δi_{Lb}, and the time between two consecutive ripples. The current ripple Δi_{Lb} depends on m_{bias} only, where m_{bias} is the bias modulation index, defined such that

$$\langle u_{\mathrm{bias}} \rangle = m_{\mathrm{bias}} U_{\mathrm{DC}}, \quad \text{for } -1 < m_{\mathrm{bias}} < 1. \tag{21}$$

The times t_0, t_2, and t_4 vary based on the output modulation index m_{out} resulting in a change in peak and RMS current. The

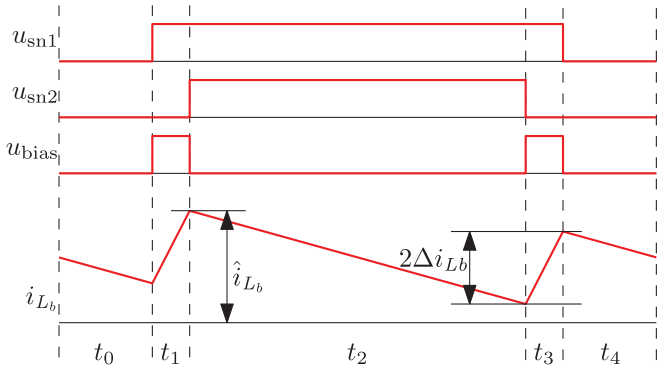

Fig. 4. Bias inductor current ripple.

output modulation index is defined as

$$\langle u_{\rm avg}\rangle = \frac{1}{2} m_{\rm out} U_{\rm DC},$$
$$\text{for} \quad -(1-|m_{\rm bias}|) \le m_{\rm out} \le (1-|m_{\rm bias}|). \quad (22)$$

To simplify calculations, an auxiliary modulation index is introduced for the output, being defined as

$$m'_{\rm out} = \frac{m_{\rm out}}{1-|m_{\rm bias}|} \quad (23)$$

which spans the usable range of the output modulation index. Depending on $m'_{\rm out}$, the peak to valley current ripple in the bias inductor varies between $2\Delta i_{Lb}$ and $4\Delta i_{Lb}$. The resulting peak current in L_b is described by

$$|\hat{i}_{L_b}| = \left[Q_{\rm Lb}\left(\frac{1}{2}+k_{\rm o}\right) + \Delta i_{Lb}\left(1+|\hat{m}'_{\rm out}|\right)\right]\hat{i}_{\rm out} \quad (24)$$

where Δi_{Lb} can be expressed in terms of $\hat{i}_{\rm out}$ as

$$\Delta i_{Lb} = \frac{2|m_{\rm bias}|k_{\rm r}}{k_{\rm Lb}}\hat{i}_{\rm out}. \quad (25)$$

The factor $k_{\rm Lb}$ is the value of L_b relative to L_f as

$$L_b = k_{\rm Lb} L_f. \quad (26)$$

The RMS current in the bias inductor is described by

$$I_{L_b} = \hat{i}_{\rm out}\sqrt{Q_{\rm Lb}^2\left(\frac{1}{2}+k_{\rm o}\right)^2 + \frac{4}{3}\left(\frac{m_{\rm bias}k_{\rm r}}{K_{Lb}}\right)^2 M^2} \quad (27)$$

with M^2, a function of $m_{\rm out}$ and $m_{\rm bias}$ given by

$$M^2 = 1 + {m'_{\rm out}}^2\left(2|m_{\rm bias}| + 2|m_{\rm out}| + 1\right). \quad (28)$$

The area-product of the bias inductor, using (24), (25), and (27), is then given by

$$A_{PLb} = \frac{L_f k_{Lb}}{\hat{B} J K_{\rm u}}\hat{i}_{\rm out}^2 \times \left[Q_{\rm Lb}\left(\frac{1}{2}+k_{\rm o}\right) + \frac{2|m_{\rm bias}|k_{\rm r}}{k_{\rm Lb}} \times \left(1+|\hat{m}'_{\rm out}|\right)\right] \times \sqrt{Q_{Lb}^2\left(\frac{1}{2}+k_{\rm o}\right)^2 + \frac{4}{3}\left(\frac{m_{\rm bias}k_{\rm r}}{k_{\rm Lb}}\right)^2 M^2}. \quad (29)$$

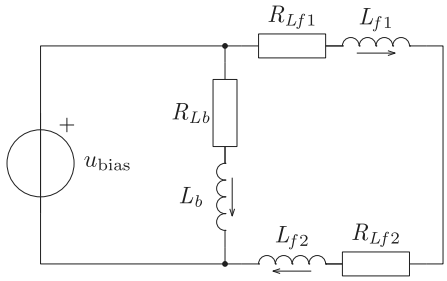

Fig. 5. Bias current distribution.

B. Current Distribution

The distribution of the bias current depends on the impedance relation between the series connected filter inductors (L_{f1} and L_{f2}) and the bias inductor L_b as shown in Fig. 5.

For the dc part of the bias current, the distribution is only dependent on the parasitic resistances of filter inductors and bias inductor. The distribution of the ac components does, however, also depend on the inductance of the components. The cutoff frequency of a typical inductor for L_b is well within the output frequency range; therefore, the ac current distribution must also be taken into account.

As the ac and dc bias current distribution are independent, either can cause high peak and RMS currents in each of the inductors. Therefore, the current distribution factors $Q_{\rm Lf}$ and $Q_{\rm Lb}$ are defined as follows:

$$Q_{\rm Lf} = \max\left(\frac{R_{Lb}}{R_{Lb}+2R_{Lf}}, \frac{L_b}{L_b+2L_f}\right) \quad (30a)$$

$$Q_{\rm Lb} = \max\left(\frac{2R_{Lf}}{R_{Lb}+2R_{Lf}}, \frac{2L_f}{L_b+2L_f}\right) \quad (30b)$$

which is the maximum of both ac and dc current distribution between the filter inductors and the bias inductor.

C. Inductor Volume

Using the current distribution factors from (30), the relative inductor volume of the ELOCC switching cell is determined. Typical values are chosen for the ripple and offset current coefficients and for the modulation indexes. The ripple current coefficient $k_{\rm r} = 0.1$, that is 10% of $\hat{i}_{\rm out}$ and the offset current coefficient $k_{\rm o} = 0.2$. An average bias voltage of 5% of $U_{\rm DC}$ is reasonable for a practical system; therefore, $m_{\rm bias} = 0.05$. The output modulation index varies sinusoidal with a maximum peak value of 0.95, for calculation, a constant value of $m_{\rm out} = 0.95$ is used. This is slightly pessimistic for the RMS current but the difference is negligible for low values of $m_{\rm bias}$.

The total inductor volume of the ELOCC switching cell, relative to a HB leg, is shown in Fig. 6. Depending on the choice of L_b, the total volume varies between a volume close to a HB leg to a volume of over a factor 4 or larger. There is an optimal relation between the inductance and resistance of L_b. This optimum is located in the valley of the graph in Fig. 6 for which

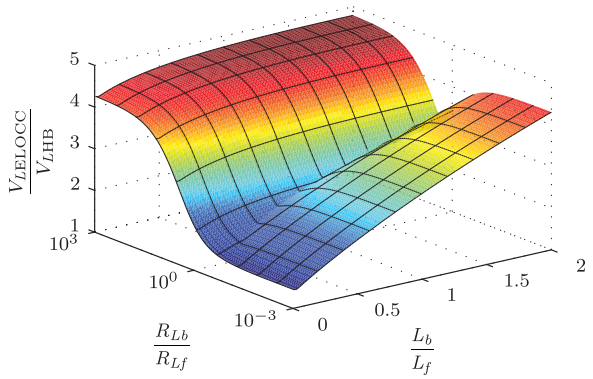

Fig. 6. ELOCC switching cell total inductor volume.

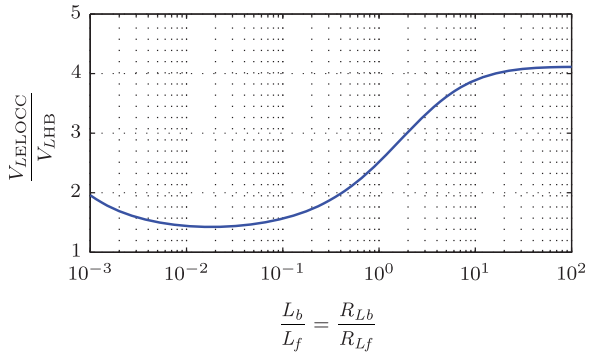

Fig. 7. ELOCC switching cell total inductor volume for an optimized bias inductor.

holds

$$\frac{L_b}{L_f} = \frac{R_{Lb}}{R_{Lf}} \tag{31}$$

or similar

$$\frac{L_b}{R_{Lb}} = \frac{L_f}{R_{Lf}}. \tag{32}$$

Therefore, the time constant of the bias inductor L_b should be chosen equal to the time constant of the filter inductors L_f. Fig. 7 depicts the total inductor volume from Fig. 6 for (32).

When choosing L_b and L_{fk}, according to (32) with $L_b/L_f \gg 1$, the volume is obtained for a standard OCC switching cell with uncoupled inductors. When choosing the bias inductor equal to the filter inductors ($L_b/L_f = 1$), a volume reduction of already 38% is obtained with respect to a standard OCC. The lowest total inductor volume is obtained when at $L_b/L_f = 0.016$, with a total volume of 1.43 with respect to a HB. For a smaller bias inductance, the total inductor volume increases; this is due to the increasing ripple in the bias inductor resulting in a higher peak and RMS current. For larger values of m_{bias}, the ripple also increases resulting in a higher optimal value for the bias inductor.

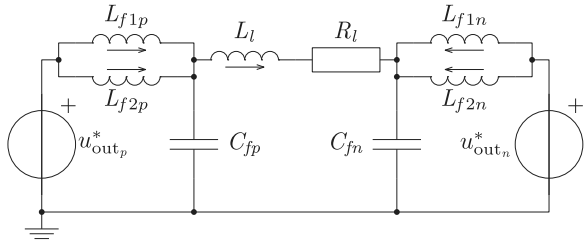

Fig. 8. ELOCC output system overview.

IV. Average Model

A high-precision power amplifier generally requires control to generate output signals that have sufficient accuracy. For control design, it is preferred to have a representative model of the system to ease design and simulations. In this section, the average model of the ELOCC switching cell is derived.

As described in Section II-A, an ELOCC switching cell can be decomposed into two decoupled systems. The output transfer function is described by

$$H_{\text{out}}(s) = \frac{i_{\text{out}}(s)}{u^*_{\text{out}}(s)} \tag{33}$$

and the bias transfer function is described by

$$H_{\text{bias}}(s) = \frac{i_{\text{bias}}(s)}{u^*_{\text{bias}}(s)}. \tag{34}$$

In both systems, the target is to have a controlled current.

In case the switching frequency T_{sw}^{-1} of the legs is much higher than the cutoff frequency of the output filter f_o, which should be the case in the ELOCC switching cell, each leg can be represented as an average voltage source $\bar{u}_{\text{snk}}$. The average voltage is given by

$$\bar{u}_{\text{sn1}} = U_{\text{DC}}\delta_{S_1} \tag{35a}$$

$$\bar{u}_{\text{sn2}} = U_{\text{DC}}(1-\delta_{S_2}) \tag{35b}$$

when the switches and diodes are considered ideal and each of the legs is operating in CCM. Using the decoupling from (3), the linear bias transfer function is obtained as

$$H_{\text{bias}}(s) = \frac{1}{2\,(sL_f + R_{Lf})} + \frac{1}{sL_b + R_{Lb}}. \tag{36}$$

When the bias inductor is chosen according to (32) and $L_b/L_f \ll 1$, the majority of the bias current flows through L_b; therefore, the left term in (36) can be neglected and H_{bias} simplifies to

$$H_{\text{bias}}(s) = \frac{1}{sL_b + R_{Lb}}. \tag{37}$$

The output transfer function is mainly dependent on the load. The output voltage is decoupled from the bias voltage/current. Therefore, the average model of the output system, in case of a full-bridge equivalent setup, simplifies to the circuit shown in Fig. 8.

The resulting output voltage is defined as

$$u^*_{\text{out}} = u^*_{\text{out}_\text{p}} - u^*_{\text{out}_\text{n}} \tag{38}$$

TABLE II
ELOCC PROTOTYPE REQUIREMENTS

Requirement	Value
$\hat{i}_{\mathrm{out}}$	12.5 A
U_{DC}	360 V
f_{sw}	187.5 kHz
L_l	3.76 mH
R_l	3.53 Ω
Open-loop bandwidth	> 5 kHz

where $u^*_{\mathrm{out_p}}$ and $u^*_{\mathrm{out_n}}$ are the output voltage setpoints of the respective positive and negative switching cell. The transfer function (33) is found to be

$$H_{\mathrm{out}}(s) = \frac{sL_l + R_l}{\frac{1}{2}s^3 L_f L_l C_f + \frac{1}{2}s^2 L_f R_l C_f + s\left(\frac{1}{2}L_f + L_l\right) + R_l} \times \frac{1}{sL_l + R_l} \tag{39}$$

which is identical to the transfer function of a full-bridge converter with $L_{\mathrm{HB}} = \frac{1}{2}L_f$. Consequently, the same output current controller can be used as in a full-bridge converter.

For frequencies well below the cutoff frequency $f \ll f_o$, the output filter transfer function is approximately 1. Then, the output transfer function simplifies to

$$H_{\mathrm{out}}(s) = \frac{1}{sL_l + R_l}. \tag{40}$$

V. EXPERIMENTAL PROTOTYPE

The performance and functionality of the ELOCC topology power stage is verified with a functional prototype. A full-bridge equivalent prototype is designed according to the specifications of an existing high-precision full-bridge current amplifier. The application of this current amplifier is a high-precision motor drive. The requirements for the prototype are given in Table II.

A. Power Stage Design

The prototype power stage is built with IXYS IXFH26N60P 26 A 600 V MOSFETs and Vishay VS-APH3006-F3 30 A 600 V diodes. The gate driver circuitry is completely reused from an existing full-bridge current amplifier.

The filter inductors L_{f1} and L_{f2} are toroidal inductors, with 220 μH inductance and 50 mΩ dc resistance. The peak current ripple in the filter inductor $\hat{\Delta}i_{Lfk}$ is 1.09 A.

The bias inductor L_b is custom designed according to (32). In case we assume all bias current flows through the bias inductor, the peak current $\hat{i}_{L_b}$ is

$$\hat{i}_{L_b} = \hat{i}_{\mathrm{bias}} + \hat{\Delta}i_{Lb} = \frac{1}{2}|\hat{i}_{\mathrm{out}}| + i_{\mathrm{offset}} + \hat{\Delta}i_{Lb} \tag{41}$$

where $\hat{i}_{\mathrm{out}} = 12.5$ A, $i_{\mathrm{offset}} \approx 3$ A, and the target peak bias inductor ripple current is set at 0.5 A. Therefore, the inductor should be rated for ≥9.75 A and have ≥30 μH inductance. The bias inductor is constructed around a smaller toroidal core than the filter inductors. The constructed inductor has 33 μH inductance and 8 mΩ dc resistance. Fig. 9 shows the bias and filter inductor of the prototype. The obtained corrected relative inductor volume is approximately between 1.4 and 1.65 with respect to a HB. The expected value of 1.69 from Fig. 7 is higher but the average bias voltage in the prototype is lower than the 5% of U_{DC} used in Fig. 7.

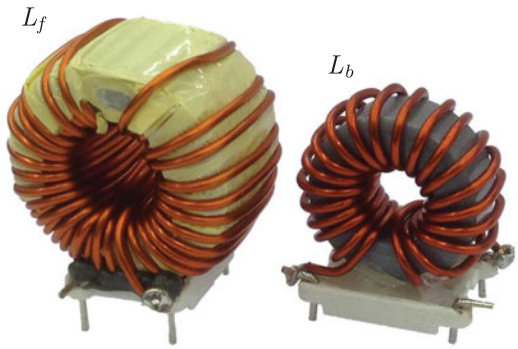

Fig. 9. Prototype filter and bias inductor.

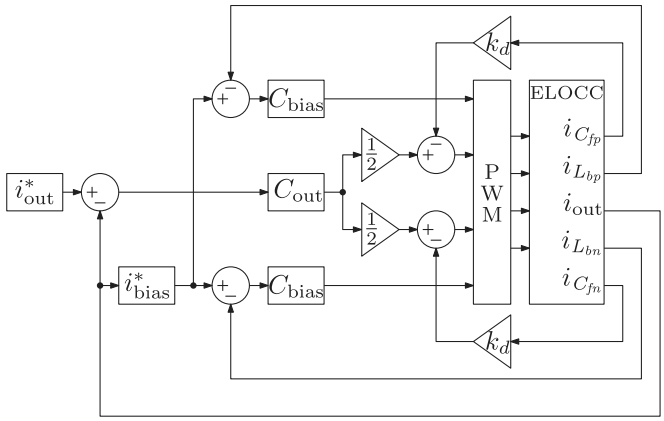

Fig. 10. ELOCC prototype control scheme overview.

B. Control

In the prototype, multiple controllers are implemented to control the ELOCC power stage. An overview of the control diagram in the prototype is shown in Fig. 10. Since the complete control scheme is implemented in an FPGA, only discrete-time controllers are used.

The output current setpoint i^*_{out} is generated internally by the FPGA. A 32-bit sine-wave lookup table is implemented to create the setpoint for the output current. The samples are addressed synchronous to the control frequency to have an optimal resolution. The frequencies that can be generated are multiples of 10 Hz.

The output current is controlled by C_{out} based on the setpoint i^*_{out} received on the input. For the output controller, a second-order continuous time controller is hand tuned. This continuous time controller is converted to a discrete-time controller using the zero-order-hold transformation in MATLAB. A symmetric triangular carrier is used in the pulse width modulation (PWM)

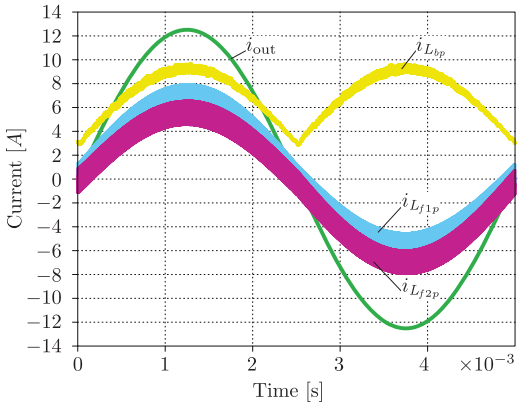

Fig. 11. Simulated prototype waveforms with an output current setpoint of 200 Hz 12.5 A_{pk}.

modulator; therefore, the output is updated twice per PWM period T_{sw}.

Based on the measured output current, a setpoint i^*_{bias} is generated for the bias current in each of the legs. The setpoint generator can be set to either constant or modulated bias current with a configurable offset current i_{offset}. The setpoint for both bias current controllers is identical.

The bias current in each of the switching cells is controlled by a bias controller C_{bias} based on the setpoint received from the bias setpoint generator. A first-order lag-lead controller has sufficient performance for the bias controller; therefore, a first-order hand-tuned controller is used. The pole of the controller is placed at 0.01 Hz and the zero is placed at 10 kHz. The gain is set to $1\frac{V}{A}$. The continuous time controller C_{bias} is converted to a discrete-time controller using the zero-order-hold transformation in MATLAB.

C. Simulation Results

The amplifier prototype is simulated using nonideal components. In the simulation, a 12.5 A_{pk} sinusoidal setpoint is used with a frequency of 200 Hz and an offset current of 3 A. An overview of the inductor currents of the positive switching cell and output current is plotted in Fig. 11. A detailed image of the switching waveforms of the positive switching cell at the peak output current is shown in Fig. 12.

As visible in Fig. 11, the current in the filter inductors is not identical. This is due to the fact that the inductance and resistance of L_b are not infinitesimal. With the selected bias and filter inductors in the prototype, the bias current through the filter inductors is about 8% of the current through L_b.

D. Measurements

Measurements are performed on the prototype to verify the functionality and performance of the ELOCC power topology. The measurement setup is shown in Fig. 13. The extra inductors can be spotted between the filter inductors.

The switching node voltages and filter inductor currents are shown in Fig. 14(a). These measurements are taken with a 5 A_{DC}

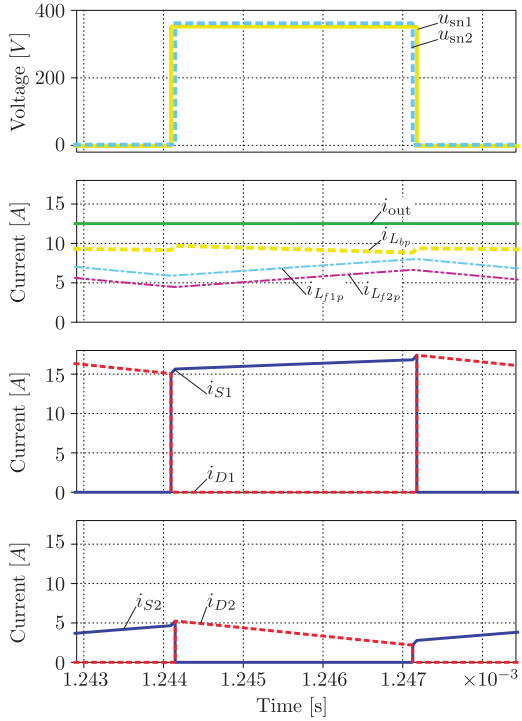

Fig. 12. Simulated prototype switching waveforms, zoomed in on a single period with $i_{\text{out}} = 12.5$ A.

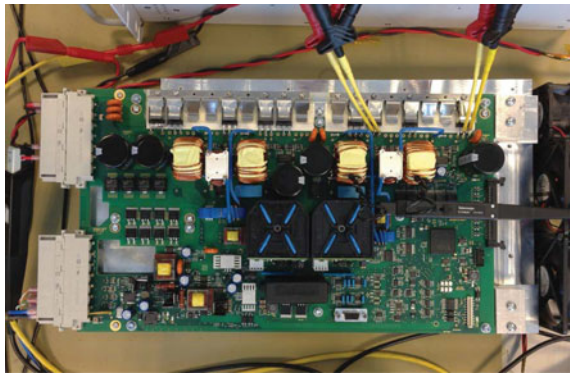

Fig. 13. ELOCC prototype measurement setup.

output current. There is a small overlap visible in the switching node voltage where both switches are ON and, thus, a positive voltage is applied across the bias inductor. This is more clear when zooming in on the edges of the switching node voltage in Fig. 14(b). The bias inductor current and output current are plotted in Fig. 15.

The low frequency behavior is shown in Fig. 16 where a 200 Hz sinusoidal output current is generated with a peak value of 12.5 A. The conditions in these measurements are equal to the conditions used in the simulation from Fig. 11. Comparing the simulation results in Fig. 11 to the measurement in Fig. 16 shows that the observed behavior is in very good agreement.

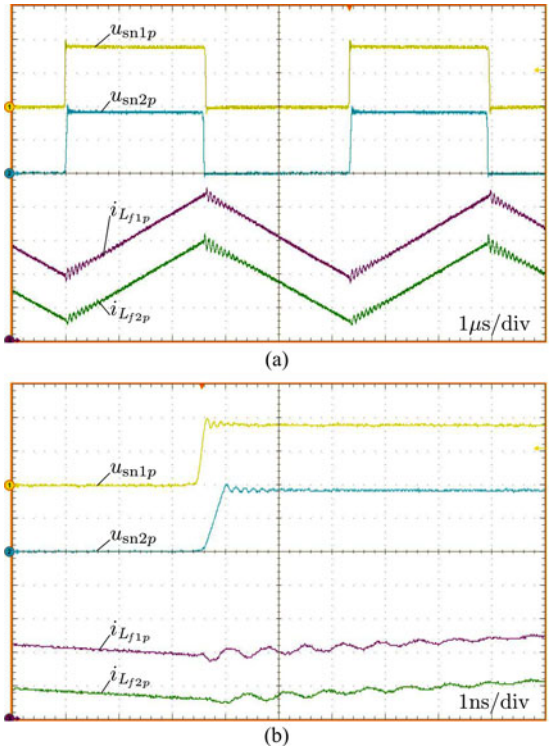

Fig. 14. Waveforms at $5\ \mathrm{A_{DC}}$ output current; (a) overview and (b) zoomed in on $u_{\mathrm{sn}}1p$ rising edge. Voltage scaling at $[200\ \mathrm{V/div}]$, current scaling at $[1\ \mathrm{A/div}]$.

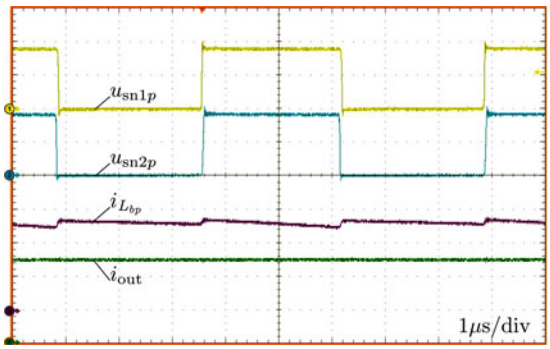

Fig. 15. Waveforms at $5\ \mathrm{A_{DC}}$ output current. Voltage scaling at $[200\ \mathrm{V/div}]$, current scaling at $[2\ \mathrm{A/div}]$.

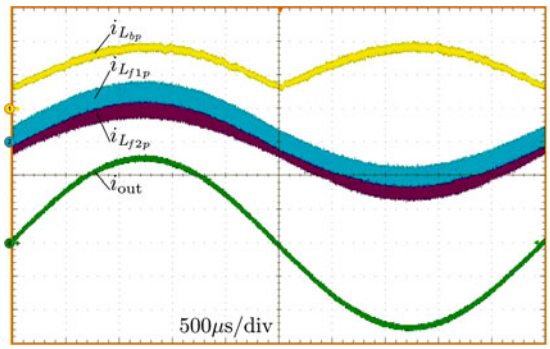

Fig. 16. Waveforms at $12.5\ \mathrm{A_{pk}}$ 200 Hz output current, current scaling is $[5\ \mathrm{A/div}]$.

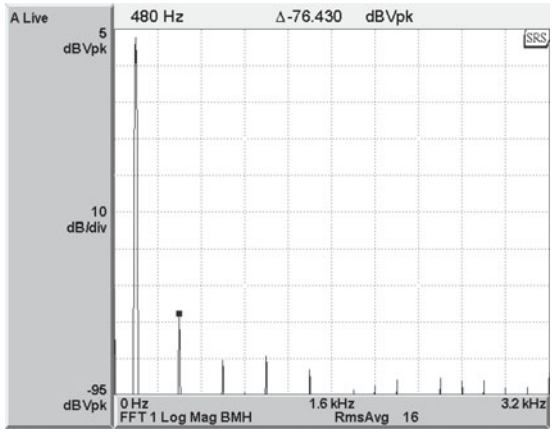

Fig. 17. Measured spectrum of i_{out} with an output current of $12.5\ \mathrm{A_{pk}}$ 160 Hz.

E. Output Linearity

The linearity of the converter is tested by measuring the distortion in the output current i_{out} with a 12.5 A 160 Hz sinusoidal output current setpoint i^*_{out}. The sinusoidal setpoint is generated internally in the FPGA with a 32-bit lookup table. The output current is measured externally with a flux-gate current sensor. This sensor has a verified spurious-free dynamic range of more than 90 dB and a bandwidth well beyond the open-loop bandwidth required for this prototype. The SR785 dynamic signal analyzer is used to analyze the harmonic content of the output current.

Measuring the distortion in an open-loop configuration shows the distortion caused by the limited PWM resolution of 9 bit. Therefore, all linearity tests are performed in closed-loop configuration. The resulting spectrum of the output current is shown in Fig. 17 where a marker is placed on the highest harmonic. The amplitude of the third harmonic is -76 dBc (dB with respect to the first harmonic), the amplitude of the fifth harmonic is -89 dBc, and the amplitude of the seventh harmonic is -87 dBc. All other harmonics have an amplitude of -90 dBc or less.

For comparison, the spurious-free dynamic range is measured of a similar amplifier with a conventional full-bridge output stage. This amplifier is highly similar to the prototype, using the same components in the end stage. Also, the same closed-loop current controller (C_{out}) and PWM modulator are used as in the prototype. Measuring the distortion in the output current under the same conditions, gives a spurious-free dynamic range of 53 dBc. This is a difference of 23dB.

Experiments show that the remaining amplitude of the harmonics in the output current of the ELOCC prototype is not caused by a ripple on the bus voltage U_{DC}. Improving the bus decoupling and reducing the 320 Hz ripple present on the bus voltage does not yield to a lower distortion in the output current.

VI. Conclusion

In this paper, a patented new high-precision amplifier topology is introduced. The advantage of the ELOCC topology compared to an equivalent half/full-bridge circuit is that it has a

much lower distortion. Also, the parallel diode of the switches is never conducting resulting in more design flexibility, as the switch and diode can be optimized separately. Moreover, the total inductor volume of an ELOCC circuit is much lower than the volume of an equivalent OCC circuit. A theoretical volume reduction of up to 72% can be obtained.

A prototype is developed of an ELOCC full-bridge equivalent power stage. The developed prototype is fully functional and capable of supplying an output current of $12.5\,\mathrm{A_{pk}}$ with an output voltage of $300\,\mathrm{V}$. The simulated behavior of the converter is in very good agreement with measured behavior of the prototype.

Without special optimization for low distortion, the spurious-free dynamic range in the output current is already $76\,\mathrm{dB}$. A comparable full-bridge amplifier has a closed-loop spurious-free dynamic range of $53\,\mathrm{dB}$. The distortion in the ELOCC prototype is most probably caused by a mismatch in voltage drop across the different switches. A lower distortion might be obtained when using MOSFETs with a lower $R_{\mathrm{DS(on)}}$ or by using IGBTs. In the prototype, the switches have a rather high resistance with a voltage drop of up to $10\,\mathrm{V}$.

REFERENCES

[1] A. Griffoni, J. van Duivenbode, D. Linten, E. Simoen, P. Rech, L. Dilillo, F. Wrobel, P. Verbist, and G. Groeseneken, "Neutron-induced failure in silicon IGBTS, silicon super-junction and SIC MOSFETs," *IEEE Trans. Nuclear Sci.*, vol. 59, no. 4, pp. 866–871, Aug. 2012.

[2] N. R. Zargari, P. D. Ziogas, and G. Joos, "A two switch high performance current regulated DC/AC converter module," in *Proc. Conf. Rec. Ind. Appl. Soc. Annu. Meet.*, 1990, pp. 929–934.

[3] G. R. Stanley and K. M. Bradshaw, "Precision DC-to-AC power conversion by optimization of the output current waveform—The half bridge revisited," *IEEE Trans. Power Electron.*, vol. 14, no. 2, pp. 372–380, 1999.

[4] Z. Yao, L. Xiao, and Y. Yan, "Dual-buck full-bridge inverter with hysteresis current control," *IEEE Trans. Ind. Electron.*, vol. 56, no. 8, pp. 3153–3160, Aug. 2009.

[5] P. Sun, C. Liu, J.-S. Lai, and C.-L. Chen, "Grid-tie control of cascade dual-buck inverter with wide-range power flow capability for renewable energy applications," *IEEE Trans. Power Electron.*, vol. 27, no. 4, pp. 1839–1849, Apr. 2012.

[6] Z. Yao and L. Xiao, "Two-switch dual-buck grid-connected inverter with hysteresis current control," *IEEE Trans. Power Electron.*, vol. 27, no. 7, pp. 3310–3318, Jul. 2012.

[7] J. Ewanchuk and J. Salmon, "A modular balancing bridge for series connected voltage sources," *IEEE Trans. Power Electron.*, vol. 29, no. 9, pp. 4712–4722, Sep. 2014.

[8] J. Schellekens, J. Duarte, H. Huisman, and M. Hendrix, "Volume reduction of opposed current converters through coupling of inductors and interleaved switching," in *Proc. IEEE 38th Annu. Conf. Ind. Electron. Soc.*, Oct. 2012, pp. 852–857.

[9] Z. Yao and G. Hu, "Comparison of dual-buck full-bridge inverter with different inductor structures," in *Proc. Asia-Pacific Power Energy Eng. Conf.*, 2011, pp. 1–3.

[10] C. Chapelsky, J. Salmon, and A. M. Knight, "High-quality single-phase power conversion by reconsidering the magnetic components in the output stage—Building a better half-bridge," *IEEE Trans. Ind. Appl.*, vol. 45, no. 6, pp. 2048–2055, Nov./Dec. 2009.

[11] J. M. Schellekens, J. L. Duarte, H. Huisman, and M. A. M. Hendrix, "High-precision current control through opposed current converters," in *Proc. 14th Eur. Conf. Power Electron. Appl.*, 2011, pp. 1–10.

[12] J. Schellekens, J. Duarte, H. Huisman, and M. Hendrix, "Harmonics in opposed current converters," in *Proc. IEEE 38th Annu. Conf. Ind. Electron. Soc.*, 2012, pp. 440–446.

[13] S. Cuk, "New magnetic structures for switching converters," vol. 19, no. 2, pp. 75–83, 1983.

[14] E. Lemmen, J. Schellekens, C. Wijnands, and J. Duarte, "The extra l opposed current converter," in *Proc. IEEE 29th Annu. Appl. Power Electron. Conf. Expo.*, Mar. 2014, pp. 1304–1311.

Erik Lemmen (S'13) received the B.Eng. degree *(cum laude)* in electrical engineering from the Fontys University of Applied Sciences, Eindhoven, The Netherlands, in 2009, and the M.Sc. degree in power electronics from the Eindhoven University of Technology, Eindhoven, in 2013, where he is currently working toward the Ph.D. degree with the group of Electromechanics and Power Electronics since 2013.

His research interests include multilevel topologies, redundancy in power converters, and high-precision amplifiers.

Jan M. Schellekens (S'09) received the B.Eng. degree in electrical engineering from Fontys University of Applied Sciences, Eindhoven, The Netherlands, in 2001, and the M.Sc. degree in power electronics from the Eindhoven University of Technology, Eindhoven, in 2007, where he is currently working toward the Ph.D. degree with the Electromechanics and Power Electronics group since 2009.

He is currently working at AME in Eindhoven. His research interests include power electronic systems for high precision systems and control design.

Cornelis G. E. Wijnands received the M.Sc. degree in power electronics from the Eindhoven University of Technology (TU Eindhoven), Eindhoven, The Netherlands, in 1994.

In 1994, he joined Prodrive B.V., Eindhoven, where he started to work on the development of power electronics and control. In September 2009, he was appointed as a part-time Assistant Professor within the Electromechanics and Power Electronics Group, TU Eindhoven, where he teaches courses on power electronics and on electrical components in vehicles. He is currently a Senior Electronics Architect with Prodrive B.V. He is also an Assistant Professor at TU Eindhoven. His professional research interests include high-precision amplifiers and automotive power electronics.

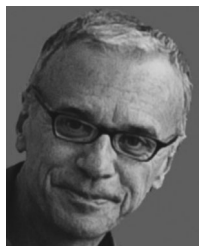

Jorge L. Duarte (M'99) received the M.Sc. degree from the Federal University of Rio de Janeiro, Rio de Janeiro, Brazil, in 1980, and the Dr.-Ing. degree from the Institute National Polytechnique de Lorraine, Nancy, France, in 1985.

In 1989, he was appointed as a Research Engineer at Philips Lighting Central Development Laboratory. Since 1990, he has been a Member of the academic staff in the Electromechanics and Power Electronics Group, Eindhoven University of Technology, Eindhoven, The Netherlands. Since October 2000, he has been a Consultant Engineer on a regular basis at high-tech industries around Eindhoven. In 2008, he was an Invited Lecturer at Zhejiang University, Hangzhou, China. His teaching and research interests include modeling, simulation, and design optimization of power electronic systems.